This article appeared as:

N. Matsuda and S. Biwa, Frequency dependence of second-harmonic generation in Lamb waves, *Journal of Nondestructive Evaluation*, Vol. 33 (2014), pp. 169-177.

Frequency dependence of second-harmonic generation in Lamb waves

Naoki Matsuda and Shiro Biwa*

Department of Aeronautics and Astronautics, Graduate School of Engineering, Kyoto University, Katsura, Nishikyo-ku, Kyoto 615-8540, Japan

Abstract

The frequency dependence of the second-harmonic generation in Lamb waves is studied theoretically and numerically in order to examine the role of phase matching for sensitive evaluation of material nonlinearity. Nonlinear Lamb wave propagation in an isotropic plate is analyzed using the perturbation technique and the modal decomposition in the neighborhood of a typical frequency satisfying the phase matching. The results show that the ratio of the amplitude of second-harmonic Lamb mode to the squared amplitude of fundamental Lamb mode grows cumulatively in a certain range of fundamental frequency for a finite propagation distance. It is also shown that the frequency for which this ratio reaches maximum is close but not equal to the phase-matching frequency when the propagation distance is finite. This feature is confirmed numerically using the finite-difference time-domain method incorporating material and geometrical nonlinearities. The fact that the amplitude of second-harmonic mode becomes high in a finite range of fundamental frequency proves robustness of the material evaluation method using second harmonics in Lamb waves.

Keywords: Nonlinear ultrasonics; Higher harmonic generation; Lamb wave; Perturbation analysis; Finite-Difference Time-Domain method

* Corresponding author: Shiro Biwa, E-mail biwa@kuaero.kyoto-u.ac.jp

1. INTRODUCTION

It is an important issue to ensure safety of structures used for industrial plants, transportation, etc., by evaluating material degradation due to creep, fatigue and plastic deformation. Ultrasonic waves are widely utilized for nondestructive evaluation (NDE) of such material damage. Foregoing studies have revealed that acoustic nonlinearity of materials, commonly manifested as higher harmonic generation, has enhanced sensitivity to material damage [1-3]. A number of studies have been carried out to explore higher harmonic generation in Lamb wave propagation to assess early stage of damage in plate-like structures [4-20]. In particular, Deng [4] experimentally observed cumulative growth of harmonic amplitude with propagation distance, i.e. cumulative harmonic generation, which is only possible under certain conditions. A perturbation approximation and modal analysis was used by de Lima and Hamilton [5] and Deng [6] to obtain the wave field of second harmonics in Lamb waves. They clarified that the conditions for cumulative growth of harmonic amplitude are (1) the phase-matching condition, and (2) non-zero power flux from the primary to the higher-harmonic Lamb wave. Deng and Pei [7] used the cumulative second-harmonic Lamb wave to evaluate fatigue damage in plates. Pruell et al. [8] examined the correlation between the acoustic nonlinearity measured with Lamb waves and the level of plastic strain in aluminum and aluminum alloy plates. Xiang et al. [9] measured thermal degradation in ferric Cr-Ni alloy steel plates using nonlinear Lamb waves. Bermes et al. [10] used a laser interferometric detection system to develop a procedure to measure material nonlinearity. Harmonic generation in Lamb waves of higher orders was analyzed theoretically by Srivastava and Lanza di Scalea [11]. Müller et al. [13] found five Lamb mode types which satisfy requirements for the cumulative second-harmonic generation, including three types in an asymptotic sense. Matsuda and Biwa [14] showed that the Lamb modes which satisfy the exact phase-matching condition are classified into four mode types including two types discussed by Müller et al. [13].

The phase-matching condition plays an important role in selecting the frequency of the fundamental mode to carry out sensitive evaluation of material nonlinearity. As demonstrated in foregoing theoretical works [6, 20] the generation and accumulation behavior of the second-harmonic Lamb mode can be qualitatively different depending on whether the fundamental frequency meets the phase matching or not. Experimentally [7, 16-18], the observed second-harmonic components have a peak at the fundamental frequency satisfying the phase matching. In practical situations, it is though difficult to tune the fundamental frequency to meet the phase matching exactly, due to the lack of precise acoustic properties of the plate or experimental setting errors. At a finite propagation distance, however, substantial growth of the second-harmonic mode, if not ideally cumulative, may be expected when the fundamental frequency meets the phase matching approximately. Therefore, it is of practical interest to explore the fundamental frequency dependence of harmonic generation in Lamb waves in a neighborhood of the phase-matching frequency.

In this paper, we present a theoretical and numerical analysis of the frequency dependence of the second-harmonic generation in Lamb waves. Nonlinear Lamb wave propagation in an isotropic plate is analyzed using the perturbation technique and the modal decomposition. The frequency dependence of surface displacement amplitude of the generated second-harmonic Lamb waves is examined in the neighborhood of a typical frequency satisfying the phase matching. The frequency

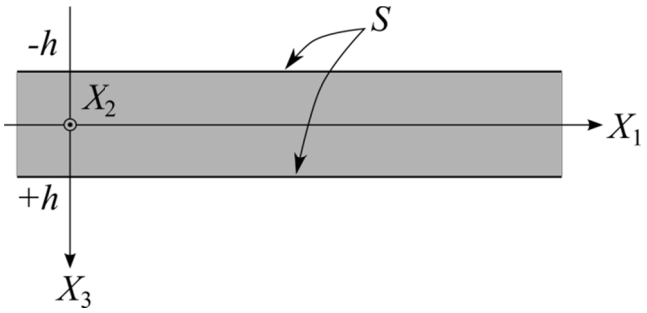

Fig.1 Geometry of an elastic plate with free boundaries

dependence is also analyzed numerically by the finite-difference time-domain (FDTD) method incorporating material and geometrical nonlinearities.

2. FORMULATION

2.1 Governing equations for an isotropic plate

Consider a plate of thickness $2h$ which is made of an isotropic and lossless elastic medium with the quadratic nonlinearity. The plate has two stress-free surfaces *S,* which are parallel to $X_1 - X_2$ plane as shown in Fig. 1. In the absence of body forces, the equation of motion, the stress-strain relation and the boundary conditions [21-24] are given by

$$\rho_0 \frac{\partial^2 U_i}{\partial t^2} - \frac{\partial P_{ij}}{\partial X_j} = 0, \quad -h < X_3 < h, \tag{1}$$

$$\begin{aligned} P_{ij} = {} & \lambda H_{kk}\delta_{ij} + \mu\left(H_{ij} + H_{ji}\right) + \lambda\left(H_{kk}H_{ij} + \tfrac{1}{2}H_{kl}H_{kl}\delta_{ij}\right) \\ & + \mu\left(H_{ik}H_{jk} + H_{ik}H_{kj} + H_{ki}H_{kj}\right) \\ & + \tfrac{1}{4}A(H_{ik} + H_{ki})(H_{kj} + H_{jk}) \\ & + B\left\{H_{kk}(H_{ij} + H_{ji}) + \tfrac{1}{2}H_{kl}(H_{kl} + H_{lk})\delta_{ij}\right\} \\ & + CH_{kk}H_{ll}\delta_{ij}, \qquad -h < X_3 < h, \end{aligned} \tag{2}$$

$$P_{i3} = 0, \qquad X_3 = \pm h, \tag{3}$$

where X_j denote the components of the reference position vector, ρ_0 the density in the reference configuration, P_{ij} the first Piola-Kirchhoff stress tensor, U_i the particle displacement vector, H_{ij} the displacement gradient tensor with respect to the reference configuration. The quantities P_{ij}, U_i and H_{ij} are considered as functions of the reference position X_j and time t. In Eq. (2), λ and μ are Lamé's elastic constants, A, B and C are the third-order elastic constants [23] and δ_{ij} is Kronecker's delta.

2.2 Linearization by perturbation analysis

The nonlinear equations (1)-(3) are solved by using the perturbation analysis and the modal decomposition. The solution U_i is assumed to be a sum of two terms:

$$U_i = U_i^{\mathrm{L}} + U_i^{\mathrm{NL}}, \tag{4}$$

where U_i^{L} is the primary solution and U_i^{NL} is the secondary solution. When weak nonlinearity

is assumed, the nonlinear equations (1)-(3) are divided into a linear homogenous and a linear non-homogeneous differential equations, which are given by

$$\rho_0 \frac{\partial^2 U_i^{\mathrm{L}}}{\partial t^2} - \frac{\partial}{\partial X_j} P_{ij}^{\mathrm{L}}(\mathbf{H}^{\mathrm{L}}) = 0, \quad -h < X_3 < h, \tag{5}$$

$$P_{i3}^{\mathrm{L}}(\mathbf{H}^{\mathrm{L}}) = 0, \quad X_3 = \pm h, \tag{6}$$

and

$$\rho_0 \frac{\partial^2 U_i^{\mathrm{NL}}}{\partial t^2} - \frac{\partial}{\partial X_j} P_{ij}^{\mathrm{L}}(\mathbf{H}^{\mathrm{NL}}) = F_i^{\mathrm{NL}}(\mathbf{H}^{\mathrm{L}}), \quad -h < X_3 < h, \tag{7}$$

$$P_{i3}^{\mathrm{L}}(\mathbf{H}^{\mathrm{NL}}) = -P_{i3}^{\mathrm{NL}}(\mathbf{H}^{\mathrm{L}}), \quad X_3 = \pm h, \tag{8}$$

where $\mathbf{H}^{\mathrm{L}}$ and $\mathbf{H}^{\mathrm{NL}}$ are the displacement gradients as to the primary solution U_i^{L} and the secondary solution U_i^{NL}, respectively. In Eqs. (5)-(8), F_i^{NL} is defined as $F_i^{\mathrm{NL}}(\mathbf{H}^{\mathrm{L}}) = \partial P_{ij}^{\mathrm{NL}}(\mathbf{H}^{\mathrm{L}}) \big/ \partial X_j$ and P_{ij}^{L} and P_{ij}^{NL} are the linear and the quadratic terms of the first Piola-Kirchhoff stress tensor:

$$P_{ij}^{\mathrm{L}}(\mathbf{H}) = \lambda H_{kk}\delta_{ij} + \mu\left(H_{ij} + H_{ji}\right), \tag{9}$$

$$\begin{aligned} P_{ij}^{\mathrm{NL}}(\mathbf{H}) = {} & \lambda\left(H_{kk}H_{ij} + \tfrac{1}{2}H_{kl}H_{kl}\delta_{ij}\right) \\ & + \mu\left(H_{ik}H_{jk} + H_{ik}H_{kj} + H_{ki}H_{kj}\right) \\ & + \tfrac{1}{4}A(H_{ik} + H_{ki})(H_{kj} + H_{jk}) \\ & + B\left\{H_{kk}(H_{ij} + H_{ji}) + \tfrac{1}{2}H_{kl}(H_{kl} + H_{lk})\delta_{ij}\right\} \\ & + CH_{kk}H_{ll}\delta_{ij}. \end{aligned} \tag{10}$$

3. ANALYSIS OF HARMONIC GENERATION IN LAMB WAVES

3.1 Modal Expansion of Lamb waves

While Eqs. (5) and (6) have Lamb mode solutions and the horizontally polarized shear mode solutions, we consider only the Lamb mode solutions as primary solutions. Here we consider the l th Lamb mode with frequency ω_0 as a solution of Eqs. (5) and (6). The primary solution is given by

$$\mathbf{U}^{\mathrm{L}} = \frac{1}{2} A_0 \overline{\mathbf{U}}^{(\kappa_l, \omega_0)}(X_3) \exp\left[i(\kappa_l X_1 - \omega_0 t)\right] + \text{c.c.}, \tag{11}$$

where c.c. stands for complex conjugate, and $\overline{\mathbf{U}}^{(\kappa_l, \omega_0)}(X_3)$ denotes the displacement profile of the l th Lamb mode whose wavenumber and angular frequency are κ_l and ω_0, respectively. The displacement profile, $\overline{\mathbf{U}}^{(\kappa_l, \omega_0)}(X_3)$, is normalized so that the displacement field $\frac{1}{2}\overline{\mathbf{U}}^{(\kappa_l, \omega_0)}(X_3)\exp\left[i(\kappa_l X_1 - \omega_0 t)\right] + \text{c.c.}$ has the unit energy flux density in the X_1 direction. The secondary solution $\mathbf{U}^{\mathrm{NL}}$ can be divided into second-harmonic term $\mathbf{U}^{2\omega}$ and DC term $\mathbf{U}^{0\omega}$. Now we consider only the second-harmonic term $\mathbf{U}^{2\omega}$, which is written as a linear combination of Lamb modes:

$$\mathbf{U}^{2\omega} = \frac{1}{2}\sum_m A_m(X_1)\overline{\mathbf{U}}^{(\kappa_m, 2\omega_0)}(X_3)\exp\left[-2i\omega_0 t\right] + \text{c.c.}, \tag{12}$$

where $\overline{\mathbf{U}}^{(\kappa_m, 2\omega_0)}$ denotes the displacement profile of the m th Lamb mode whose wave number and frequency are κ_m and $2\omega_0$, respectively. Suppose that the m th Lamb mode is a propagating mode. The modal amplitude $A_m(X_1)$ is given by [5, 25],

$$A_m(X_1) = \begin{cases} \dfrac{f_m^{\text{surf}} + f_m^{\text{vol}}}{4P_{mm}} \cdot \mathrm{e}^{2i\kappa_l X_1} \cdot \dfrac{\mathrm{e}^{i(\kappa_m - 2\kappa_l)X_1} - 1}{i(\kappa_m - 2\kappa_l)}, & \kappa_m \neq 2\kappa_l, \\ \dfrac{f_m^{\text{surf}} + f_m^{\text{vol}}}{4P_{mm}} \cdot \mathrm{e}^{2i\kappa_l X_1} \cdot X_1, & \kappa_m = 2\kappa_l, \end{cases} \tag{13}$$

where

$$P_{mm} = \frac{1}{4}\int_{-h}^{h}\left(-\frac{\overline{\boldsymbol{\sigma}}^{(\kappa_m, 2\omega_0)}}{2}\frac{\overline{\mathbf{V}}^{(\kappa_m, 2\omega_0)*}}{2} - \frac{\overline{\boldsymbol{\sigma}}^{(\kappa_m, 2\omega_0)*}}{2}\frac{\overline{\mathbf{V}}^{(\kappa_m, 2\omega_0)}}{2}\right)\cdot\mathbf{e}_1 dX_3, \tag{14}$$

$$f_m^{\text{surf}} = -\left\{\frac{\overline{\mathbf{p}}^{2\omega}}{2}\frac{\overline{\mathbf{V}}^{(\kappa_m, 2\omega_0)*}}{2}\right\}\cdot\mathbf{e}_1\Bigg|_{X_3=-h}^{X_3=h}, \tag{15}$$

$$f_m^{\text{vol}} = \int_{-h}^{h}\frac{\overline{\mathbf{f}}^{2\omega}}{2}\cdot\frac{\overline{\mathbf{V}}^{(\kappa_m, 2\omega_0)*}}{2}dX_3. \tag{16}$$

where $\mathbf{e}_1$ is the unit vector in the X_1 direction, $\overline{\mathbf{V}}^{(\kappa_m, 2\omega_0)}(X_3)$ the velocity profile and $\overline{\boldsymbol{\sigma}}^{(\kappa_m, 2\omega_0)}(X_3)$ the stress profile of the m th Lamb mode. The superscripts of an asterisk denote the complex conjugate. In Eqs. (15) and (16), $\overline{\mathbf{p}}^{2\omega}$ and $\overline{\mathbf{f}}^{2\omega}$ are the second-harmonic terms of $\mathbf{P}^{\text{NL}}$ and $\mathbf{F}^{\text{NL}}$, which are defined as

$$\begin{aligned}\mathbf{P}^{\text{NL}}\left(\mathbf{H}^{\text{L}}(X_1, X_3, t)\right) &= \frac{1}{2}\overline{\mathbf{p}}^{2\omega}(X_3)\exp\left[2i(\kappa_l X_1 - \omega_0 t)\right] \\ &\quad + \frac{1}{2}\overline{\mathbf{p}}^{0\omega}(X_3)\exp[i(\kappa_l - \kappa_l^*)X_1] + \text{c.c.},\end{aligned} \tag{17}$$

$$\begin{aligned}\mathbf{F}^{\text{NL}}\left(\mathbf{H}^{\text{L}}(X_1, X_3, t)\right) &= \frac{1}{2}\overline{\mathbf{f}}^{2\omega}(X_3)\exp\left[2i(\kappa_l X_1 - \omega_0 t)\right] \\ &\quad + \frac{1}{2}\overline{\mathbf{f}}^{0\omega}(X_3)\exp[i(\kappa_l - \kappa_l^*)X_1] + \text{c.c.}\end{aligned} \tag{18}$$

Note that P_{mm} is $h/2$ regardless of m, since the energy flux density of $\overline{\mathbf{U}}^{(\kappa_m, 2\omega_0)}(X_3)$ is normalized. Let $R_m(X_1)$ be the ratio of the in-plane displacement amplitude of the second-harmonic Lamb mode to the squared in-plane displacement amplitude of the fundamental Lamb mode on the surface ($X_3 = h$), i.e.,

$$R_m(X_1) = \frac{\left|A_m(X_1)\overline{\mathbf{U}}^{(\kappa_m, 2\omega_0)}(h)\cdot\mathbf{e}_1\right|}{\left|A_0\mathrm{e}^{i\kappa_l X_1}\overline{\mathbf{U}}^{(\kappa_l, \omega_0)}(h)\cdot\mathbf{e}_1\right|^2}. \tag{19}$$

This ratio can be decomposed as

$$R_m(X_1) = X_1 S_m T_m(X_1), \tag{20}$$

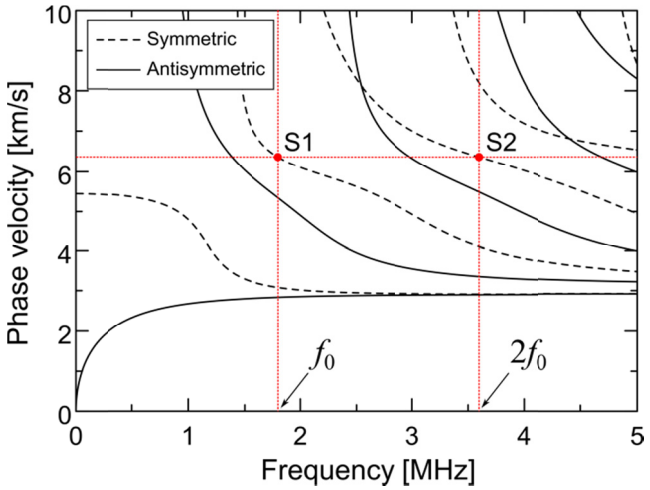

Fig. 2 Dispersion curves of Lamb waves for an aluminum plate with a thickness of 2.0 mm and the mode pair which satisfies the phase-matching condition

where

$$S_m = \left| \frac{f_m^{\mathrm{surf}} + f_m^{\mathrm{vol}}}{4P_{mm}} \right| \cdot \frac{\left| \overline{\mathbf{U}}^{(\kappa_m, 2\omega_0)}(h) \cdot \mathbf{e}_1 \right|}{\left| A_0 \overline{\mathbf{U}}^{(\kappa_l, \omega_0)}(h) \cdot \mathbf{e}_1 \right|^2}, \tag{21}$$

$$T_m(X_1) = \begin{cases} \left| \mathrm{sinc}\left[\dfrac{(\kappa_m - 2\kappa_l)}{2} X_1 \right] \right|, & \kappa_m \neq 2\kappa_l, \\ 1, & \kappa_m = 2\kappa_l. \end{cases} \tag{22}$$

In the above expression, S_m contains a factor representing the power flux from the fundamental Lamb mode to the second-harmonic Lamb mode as discussed by e.g., de Lima and Hamilton [5]. The factor $T_m(X_1)$ determines the deviation from the linear dependence on the propagation distance.

3.2 Example and Discussion

The first-order symmetric (S1) Lamb mode with frequency ω_0 and the second-order symmetric (S2) Lamb mode with frequency $2\omega_0$ are selected as the fundamental and the second-harmonic Lamb modes. For this pair, R_m, S_m and T_m in a 2 mm-thick aluminum plate are calculated for the fundamental frequency $f_0 = \omega_0/(2\pi)$ from 1.6 to 2.0 MHz. Note that the mode pair of 1.8 MHz S1 mode and 3.6 MHz S2 mode satisfies the phase-matching condition as shown in the phase velocity-frequency diagram in Fig. 2 (symmetric modes with dominant longitudinal displacements [13, 14]). This is also the pair of Lamb modes which has been used in foregoing experimental investigations [8, 10, 19, 20]. The material parameters of aluminum are shown in Table 1 [26]. In Fig. 3, R_m, S_m and T_m are shown as functions of the fundamental frequency f_0. Figures 3(a) and 3(c) show the results when the propagation distance is varied from 50 to 150 mm. The vertical line in Fig. 3(a) shows the exact phase-matching frequency.

Table 1 Physical properties of aluminum and steel

	ρ_0 [kg/m^3]	λ [GPa]	μ [GPa]	A [GPa]	B [GPa]	C [GPa]
Aluminum	2700	56.0	26.5	-408	-197	-114
Steel	7874	111	82.1	-708	-282	-179

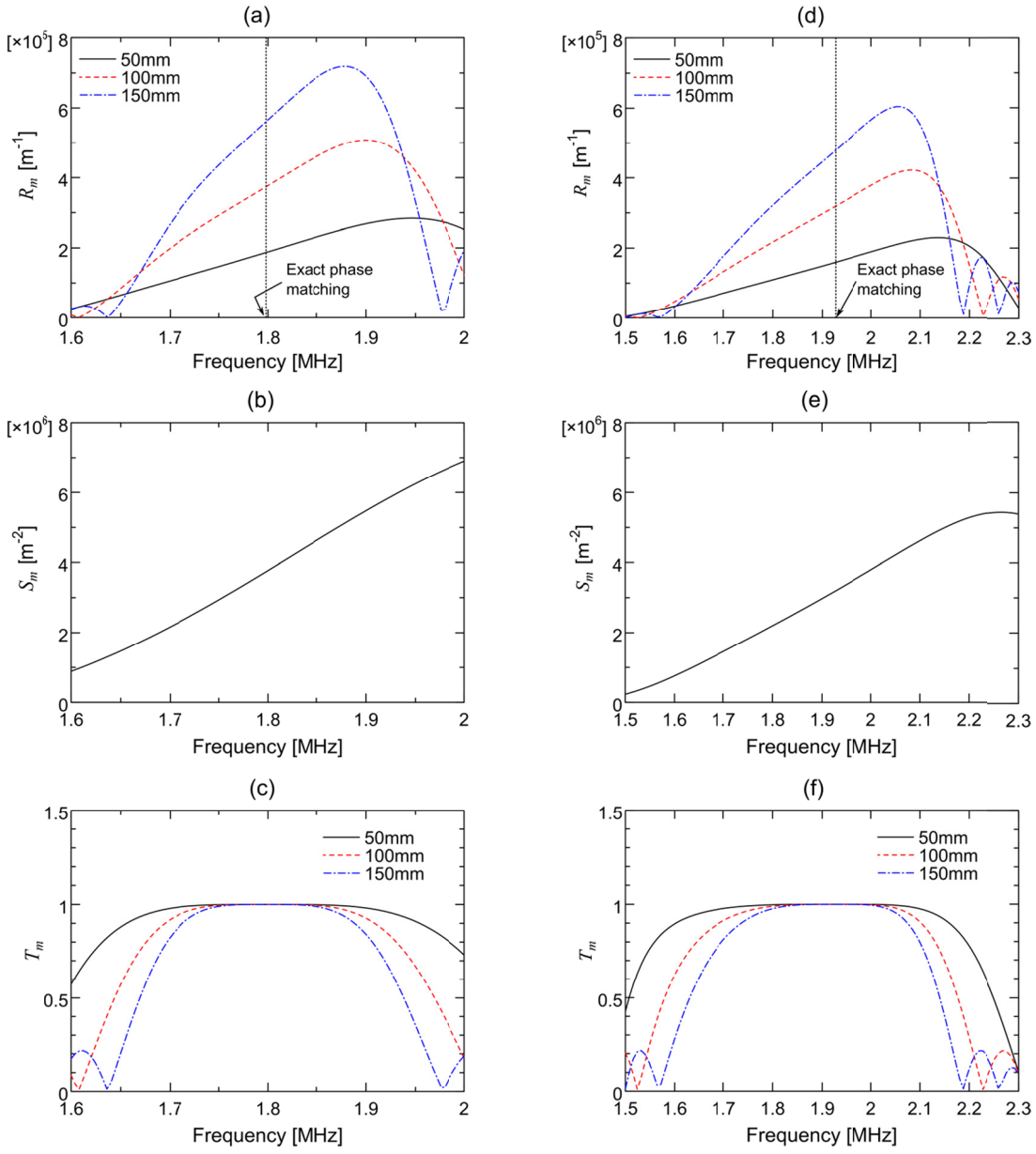

Fig. 3 (a) Variation of the ratio of the in-plane displacement amplitude of the second-harmonic Lamb mode to the squared in-plane displacement amplitude of the fundamental Lamb mode on the surface R_m and its components (b) S_m and (c) T_m with the fundamental frequency of Lamb wave for an aluminum plate, and (d), (e), (f) those for a steel plate, respectively.

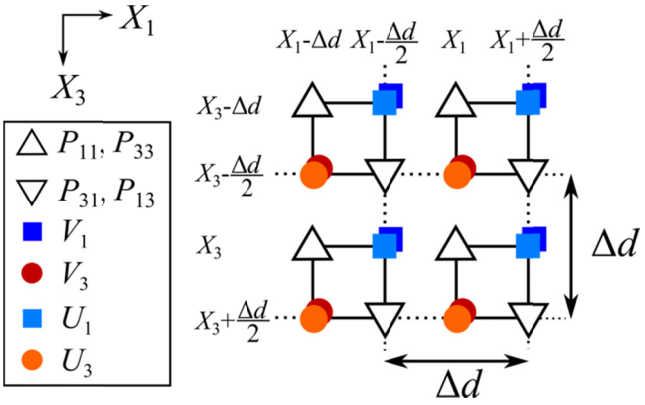

Fig. 4 The FDTD grid for the nonlinear simulation

Considering T_m as a function of the fundamental frequency, it acts as a bandpass filter with a flat passband at the phase-matching frequency 1.8 MHz as shown in Fig. 3(c). The width of the passband is determined by the propagation distance of Lamb waves. Therefore, when the fundamental frequency is within the passband, R_m grows in proportion with the propagation distance X_1, and its fundamental frequency dependence is mainly determined by that of S_m, since T_m is almost constant in the passband. Therefore, the frequency for which R_m has the maximum value is determined not only by the phase-matching condition but also by other factors represented by S_m given in Eq. (21), i.e., the power flux from the fundamental Lamb mode to the second-harmonic Lamb mode.

To examine the influence of the difference of material on the harmonic generation, R_m, S_m and T_m in a 2 mm-thick steel plate are also calculated for the fundamental frequency from 1.5 to 2.3 MHz and shown in Fig. 3 (d), (e) and (f), respectively. The material parameters of steel are shown in Table 1 [26]. Note that the mode pair of 1.93 MHz S1 mode and 3.86 MHz S2 mode satisfies the phase-matching condition in a steel plate with 2mm thickness. We see from Fig. 3 (c) and (f) that the passband for a steel plate is about twice as wide as that for an aluminum plate, which indicates that the tuning of the fundamental frequency for cumulative second-harmonic measurements is less severe for steel.

4. NUMERICAL SIMULATION

4.1 Finite Difference Formulation for Nonlinear Elastic Media

To confirm the results of the perturbation analysis, we also conduct numerical simulations. Recently, Matsuda and Biwa [27] have extended the elastodynamic finite-difference time-domain (FDTD) scheme [28] to incorporate the stress-strain nonlinearity as well as the kinematical nonlinearity. Assuming two-dimensional plane-strain motion in the $X_1 - X_3$ plane, the second-order differential equation in Eq. (1) is rewritten into a set of first-order differential equations. Nodes of the particle displacements, the velocities and the first Piola-Kirchoff stresses are arranged in the grid for the nonlinear simulations as shown in Fig. 4 where Δd denotes the

grid size. The displacements and the stresses (U_1, U_3, P_{11}, P_{33}, P_{13}, P_{31}) are updated when the time step index is integer and the velocities (V_1, V_3) are updated when it is half-integer. The updated displacements are given as follows,

$$U_1{}^n(i+1/2,j) = U_1{}^{n-1}(i+1/2,j) + \Delta t V_1{}^{n-1/2}(i+1/2,j), \tag{23}$$

$$U_3{}^n(i,j+1/2) = U_3{}^{n-1}(i,j+1/2) + \Delta t V_3{}^{n-1/2}(i,j+1/2), \tag{24}$$

where i and j are the indices of a grid point in the X_1 and X_3 direction, respectively. The superscript index n denotes the time step and Δt is its increment. The components of the first Piola-Kirchhoff stress tensor are given by

$$\begin{aligned} P_{11}{}^n(i,j) &= c_{11}U_{1,1}{}^n(i,j) + c_{13}U_{3,3}{}^n(i,j) \\ &\quad + d_1\left[U_{1,1}{}^n(i,j)\right]^2 \\ &\quad + d_2\left[2U_{1,1}{}^n(i,j) + U_{3,3}{}^n(i,j)\right]U_{3,3}{}^n(i,j) \\ &\quad + d_3\left\{\left[U_{1,3}{}^n(i,j)\right]^2 + \left[U_{3,1}{}^n(i,j)\right]^2\right\} \\ &\quad + d_4U_{1,3}{}^n(i,j)U_{3,1}{}^n(i,j), \end{aligned} \tag{25}$$

$$\begin{aligned} P_{33}{}^n(i,j) &= c_{11}U_{3,3}{}^n(i,j) + c_{13}U_{1,1}{}^n(i,j) \\ &\quad + d_1\left[U_{3,3}{}^n(i,j)\right]^2 \\ &\quad + d_2\left[U_{1,1}{}^n(i,j) + 2U_{3,3}{}^n(i,j)\right]U_{1,1}{}^n(i,j) \\ &\quad + d_3\left\{\left[U_{1,3}{}^n(i,j)\right]^2 + \left[U_{3,1}{}^n(i,j)\right]^2\right\} \\ &\quad + d_4U_{1,3}{}^n(i,j)U_{3,1}{}^n(i,j), \end{aligned} \tag{26}$$

$$\begin{aligned} P_{13}{}^n(i+1/2,j+1/2) &= c_{55}\left[U_{1,3}{}^n(i+1/2,j+1/2) + U_{3,1}{}^n(i+1/2,j+1/2)\right] \\ &\quad + \left[U_{1,1}{}^n(i+1/2,j+1/2) + U_{3,3}{}^n(i+1/2,j+1/2)\right] \\ &\quad \times\left[2d_3U_{1,3}{}^n(i+1/2,j+1/2) + d_4U_{3,1}{}^n(i+1/2,j+1/2)\right], \end{aligned} \tag{27}$$

$$\begin{aligned} P_{31}{}^n(i+1/2,j+1/2) &= c_{55}\left[U_{1,3}{}^n(i+1/2,j+1/2) + U_{3,1}{}^n(i+1/2,j+1/2)\right] \\ &\quad + \left[U_{1,1}{}^n(i+1/2,j+1/2) + U_{3,3}{}^n(i+1/2,j+1/2)\right] \\ &\quad \times\left[2d_3U_{3,1}{}^n(i+1/2,j+1/2) + d_4U_{1,3}{}^n(i+1/2,j+1/2)\right], \end{aligned} \tag{28}$$

where the subscripts following a comma denote the partial derivatives with respect to the material coordinate. The coefficients c_{11}, c_{13}, c_{55}, d_1, d_2, d_3 and d_4 are the linear combinations of the second- and third-order elastic constants of isotropic media defined as follows,

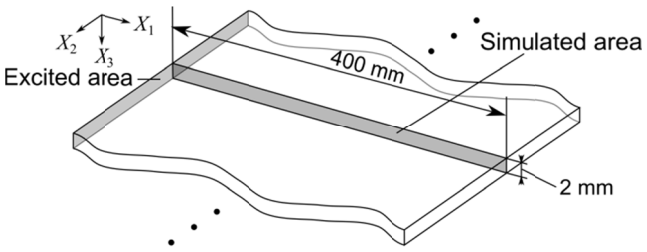

Fig. 5 The configuration of the model for numerical calculation

$$
\begin{aligned}
&c_{11} = \lambda + 2\mu, \quad c_{13} = \lambda, \quad c_{55} = \mu, \\
&d_1 = \frac{3}{2}\lambda + 3\mu + A + 3B + C, \\
&d_2 = \frac{1}{2}\lambda + B + C, \\
&d_3 = \frac{1}{2}\lambda + \mu + \frac{1}{4}A + \frac{1}{2}B, \\
&d_4 = \mu + \frac{1}{2}A + B.
\end{aligned}
\tag{29}
$$

The equation of motion gives the velocities of the next time step,

$$V_1^{n+1/2}(i+1/2, j) = V_1^{n-1/2}(i+1/2, j) + \frac{\Delta t}{\rho_0}\left[P_{11,1}{}^{n}(i+1/2, j) + P_{13,3}{}^{n}(i+1/2, j)\right], \tag{30}$$

$$V_3^{n+1/2}(i, j+1/2) = V_3^{n-1/2}(i, j+1/2) + \frac{\Delta t}{\rho_0}\left[P_{31,1}{}^{n}(i, j+1/2) + P_{33,3}{}^{n}(i, j+1/2)\right]. \tag{31}$$

Explicit expressions for the spatial gradients of the displacements in Eqs. (25) to (28) and the first Piola-Kirchhoff stress tensor in Eqs. (30) and (31) are lengthy, and hence they will not be presented here (the details are described by Matsuda and Biwa [27]). Using Eqs. (23)-(31), we alternately calculate the displacements/stresses and the velocities according to when the time step index is integer or half-integer, respectively. The stress-free boundaries are incorporated using the zero-stress formulation [28].

4.2 Numerical Analysis of Nonlinear Lamb Wave Propagation

Specification of the model used for the numerical analysis is shown in Fig. 5. The length and the thickness of the plate are 400 mm and 2 mm, respectively. The upper and lower surfaces $(X_3 = \pm h)$ are assumed traction-free. The plate is assumed to be made of aluminum and its material properties are listed in Table 1. The time step increment and grid size are Δt = 3.15 ns and Δd = 50 μm, respectively.

The fundamental Lamb wave is excited from the left end (X_1 = 0) of the plate, by prescribed tractions given as

$$
\begin{aligned}
P_{11}(0, X_3, t) &= A_0 W(t)\,\mathrm{Re}\left[\bar{\sigma}_{11}^{(\kappa_I, \omega_0)}(X_3)\exp(-2\pi i f_0 t)\right], \\
P_{13}(0, X_3, t) &= A_0 W(t)\,\mathrm{Re}\left[\bar{\sigma}_{13}^{(\kappa_I, \omega_0)}(X_3)\exp(-2\pi i f_0 t)\right],
\end{aligned}
\tag{32}
$$

where

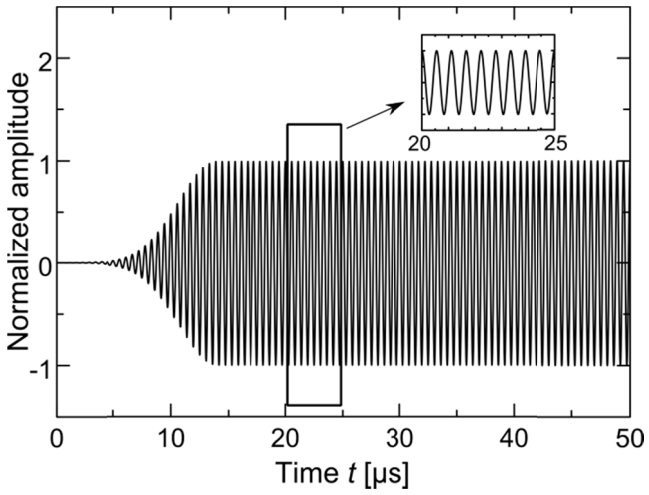

Fig. 6 Time domain waveform of excitation

$$W(t)=\begin{cases}\exp\left[-\left(\dfrac{t-t_0}{t_1}\right)^2\right], & 0\le t<t_0,\\ 1, & t_0<t,\end{cases} \tag{33}$$

where t_0 = 14 [μs] and t_1 = 4.7 [μs] in this study. The thickness profiles $\overline{\sigma}_{11}^{(\kappa_l,\omega_0)}(X_3)$ and $\overline{\sigma}_{13}^{(\kappa_l,\omega_0)}(X_3)$ are given as the S1 mode stress profiles by the linear theory of Lamb waves. Figure 6 illustrates the input waveform $P_{11}(0,0,t)/P_{11\max}$, where $P_{11\max}$ is the maximum value of $P_{11}(0,0,t)$ with respect to t. The amplitude of the prescribed traction rises gradually with time and achieves a constant level, which enables the simulation of the response of the plate to a steady-state monochromatic excitation. The simulation is performed by increasing the fundamental frequency f_0 from 1.6 MHz to 2.0 MHz in steps of 0.01 MHz. In each simulation, the fundamental Lamb mode amplitude A_0 is set so that the energy flux density of the excited fundamental Lamb mode is equal to that of the longitudinal wave with frequency 1.8 MHz and displacement amplitude 1.0 nm. Collecting the computed in-plane displacement waveforms at the upper surface of the plate, we obtain the time domain waveforms at different distances from the excitation point. These waveforms can be considered as a spatial-temporal distribution of the in-plane displacement $U_1(X_1,t)$. This distribution is windowed by a temporal and spatial window function and analyzed by the two-dimensional Fourier transform. The transform $F_{U_1}(K,f)$ is calculated as

$$F_U(K,f)=\int_{-\infty}^{\infty}\int_{-\infty}^{\infty}G_{\overline{X},\overline{t}}(X_1,t)U(X_1,t)\mathrm{e}^{2i\pi(KX_1-ft)}dX_1dt, \tag{34}$$

where K and f are the wavenumber (inverse of wave length) and the frequency, respectively, and $G_{\overline{X},\overline{t}}(X_1,t)$ is a Gaussian window function:

$$G_{\overline{X},\overline{t}}(X_1,t)=\exp\left[-\left(\frac{X_1-\overline{X}}{\xi}\right)^2-\left(\frac{t-\overline{t}}{\tau}\right)^2\right]. \tag{35}$$

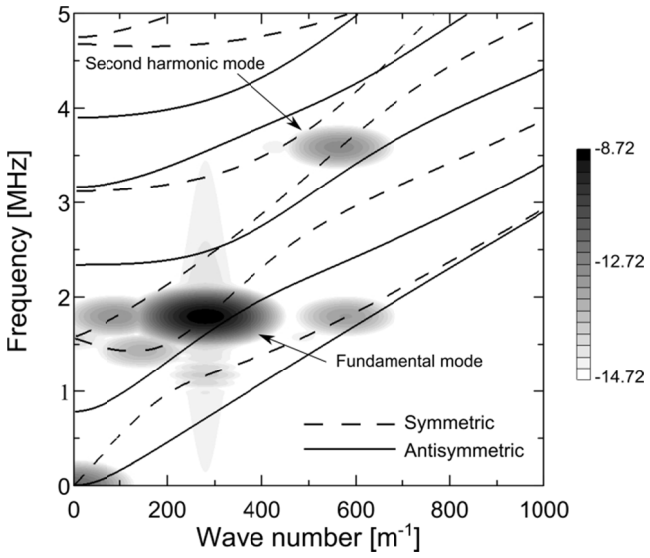

Fig. 7 $f-K$ **distribution of** $\log_{10}\left[F_{U_1}(K,f)\right]$ **at the propagation distance of 100 mm**

The window function has four parameters which determine their shape and position, including the spatial position of the window function $\overline{X}$, corresponding to the propagation distance of the wave.

4.3 Results and discussion

Figure 7 shows the result of the two-dimensional Fourier transform when the excitation frequency is 1.8 MHz. The window parameters are $\bar{t}$ = 180 [μs], τ = 3.3 [μs] and ξ = 6.7 [mm], and the spatial position of the window function $\overline{X}$ is 100 mm. It is noted that the peaks in Fig. 7 are not sharp but show some spread because of the finite temporal and spatial widths of the window function. The solid and dashed lines in Fig. 7 denote the dispersion curves of the linear theory of Lamb waves. The amplitude of the second-harmonic Lamb wave (S2 mode, 3.6 MHz) and that of the fundamental mode (S1 mode, 1.8 MHz) can be obtained from Fig. 7. We calculate the ratio of the second harmonic amplitude and the squared fundamental wave amplitude as R_m, and shown in Fig. 8 as functions of the spatial position of the window function $\overline{X}$, for different fundamental frequencies. The symbols in Fig. 8 show the results of the FDTD simulations, while the lines are calculated by the perturbation analysis. The amplitude ratio R_m grows proportionally with propagation distance when the frequency of fundamental Lamb mode is 1.8 MHz, but cumulative growth can also be seen at the neighboring frequencies. In particular, for 1.9 MHz R_m can be even higher at finite distances. This shows that second-harmonic Lamb waves can be generated cumulatively when the phase-matching condition is satisfied in an approximate sense.

In Fig. 9 the plotted symbols denote R_m as functions of the fundamental Lamb mode frequency when the spatial position of the window function $\overline{X}$ is 50, 100, and 150 mm. The curves denote the results of the perturbation analysis shown in Fig. 3(a), and the vertical line

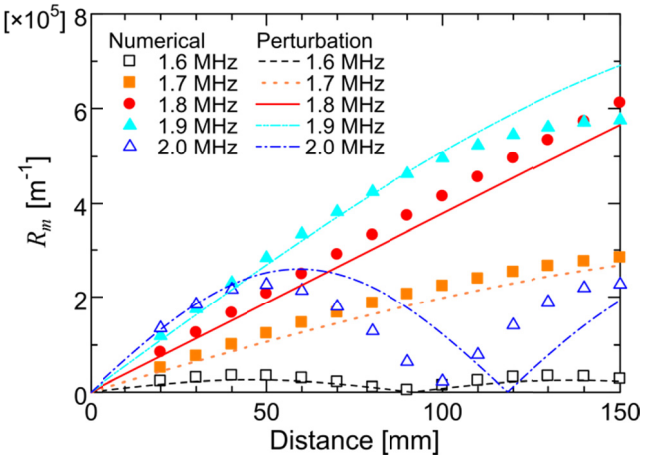

Fig. 8 Variation of the amplitude ratio R_m with propagation distance

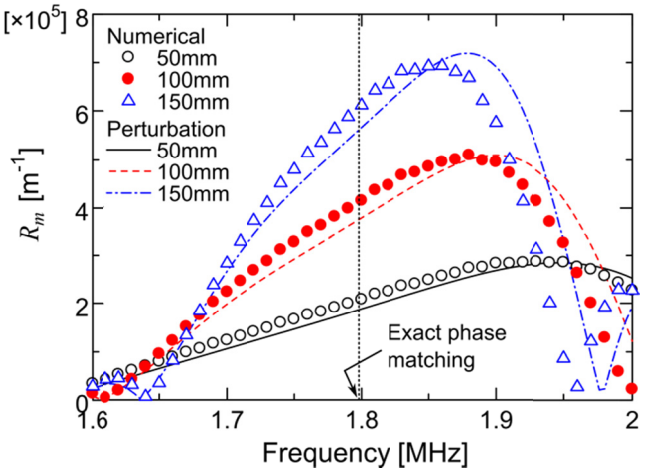

Fig. 9 Variation of the amplitude ratio R_m with fundamental frequency of Lamb waves

shows the phase-matching frequency. In Figs. 8 and 9, the numerical results by the FDTD method show fair agreement with those of the perturbation analysis, although there are some discrepancies probably due to the numerical dispersion inherent in the FDTD method. As shown above by the perturbation analysis, the results of FDTD simulations also show that R_m reaches its maximum when the fundamental frequency is close but not equal to the phase-matching frequency.

Practically, it is an important issue to select the fundamental frequency of Lamb mode which generates a high R_m to assess the material nonlinearity sensitively in the early stage of degradation. This study has revealed that R_m can become relatively high even when the fundamental frequency is not exactly equal to the phase-matching frequency. This is a useful fact in practical situations. For example, even if the acoustic properties or the thickness of the plate are not exactly known and the fundamental frequency chosen in the measurement is different from the true phase-matching frequency, nearly cumulative growth of second harmonic can be expected.

This fact shows robustness of the material evaluation method using second harmonics in Lamb waves. It should be noted, however, that the linear dependence of the second-harmonic amplitude on the propagation distance can be violated when the fundamental frequency is off the phase matching: the frequency bandwidth in which the linear dependence holds is determined by the propagation distance as shown in Fig. 3(c) for aluminum and Fig. 3 (f) for steel. This needs to be accounted for when material nonlinearity is to be quantitatively evaluated from the measurement.

It is finally commented that in contrast to the monochromatic excitation simulated here, practical measurements are more often performed using a tone-burst excitation of the fundamental Lamb wave which has a finite frequency bandwidth. As far as weak nonlinearity holds, it is expected that the dependence of the observed second-harmonic amplitude on the center frequency of the tone-burst is given by a (kind of) average of the results shown here for monochromatic excitation over the frequency bandwidth. As a result, peaks of the second-harmonic amplitude for varying center frequency will be less sharp than those shown here, and the null points of the second-harmonic amplitude (as seen at 1.64 MHz and 1.96 MHz for 150 mm in Fig. 9) will disappear.

5. CONCLUSION

An analysis of the fundamental frequency dependence of the second-harmonic generation in Lamb waves has been shown in this paper. The ratio of the amplitude of the second-harmonic Lamb mode to the squared amplitude of the fundamental Lamb mode has been calculated by the perturbation analysis and modal decomposition. The second-harmonic amplitude can grow cumulatively in a certain range of fundamental frequency when the propagation length is finite. The analysis reveals that the frequency for which the second harmonic Lamb mode reaches maximum is close but not equal to the phase-matching frequency in a precise sense. This feature has been confirmed numerically using the finite-difference time-domain method incorporating the material and geometrical nonlinearities. The fact that the second-harmonic amplitude becomes high in a certain fundamental frequency range proves robustness of the material evaluation method using second harmonics in Lamb waves.

6. ACKNOWLEDGEMENTS

This work has been supported by JSPS KAKENHI Grant Numbers 24·2517 and 25289005.

REFERENCES

[1] Cantrell JH, Yost WT (2001) Nonlinear ultrasonic characterization of fatigue microstructures. Int J Fatig 23:487-490. doi: 10.1016/S0142-1123(01)00162-1

[2] Herrmann J, Kim J-Y, Jacobs LJ, Qu J, Littles JW, Savage MF (2006) Assessment of material damage in a nickel-base superalloy using nonlinear Rayleigh surface waves. J Appl Phys 99:124913. doi: 10.1063/1.2204807

[3] Kim J-Y, Jacobs LJ, Qu J, Littles JW (2006) Experimental characterization of fatigue damage in a nickel-base superalloy using nonlinear ultrasonic waves. J Acoust Soc Am 120:1266-1273. doi: 10.1121/1.2221557

[4] Deng M (1999) Cumulative second-harmonic generation of Lamb-mode propagation in a solid plate. J Appl Phys 85:3051-3058. doi: 10.1063/1.369642

[5] de Lima WJN, Hamilton MF (2003) Finite-amplitude waves in isotropic elastic plates. J Sound Vib 265:819-839. doi: 10.1016/S0022-460X(02)01260-9

[6] Deng M (2003) Analysis of second-harmonic generation of Lamb modes using a modal analysis approach. J Appl Phys 94:4152-4159. doi: 10.1063/1.1601312

[7] Deng M, Pei J (2007) Assessment of accumulated fatigue damage in solid plates using nonlinear Lamb wave approach. Appl Phys Lett 90:121902. doi: 10.1063/1.2714333

[8] Pruell C, Kim J-Y, Qu J, Jacobs LJ (2007) Evaluation of plasticity driven material damage using Lamb waves. Appl Phys Lett 91:231911. doi: 10.1063/1.2811954

[9] Xiang Y, Deng M, Xuan F-Z, Liu C-J (2011) Experimental study of thermal degradation in ferritic Cr-Ni alloy steel plates using nonlinear Lamb waves. NDT&E Int 44:768-774. doi: 10.1016/j.ndteint.2011.08.005

[10] Bermes C, Kim J-Y, Qu J, Jacobs LJ (2007) Experimental characterization of material nonlinearity using Lamb waves. Appl Phys Lett 90:021901. doi: 10.1063/1/2431467

[11] Srivastava A, Lanza di Scalea F (2009) On the existence of antisymmetric or symmetric Lamb waves at nonlinear higher harmonics. J Sound Vib 323:932-943. doi: 10.1117/12.815448

[12] Xiang Y, Deng M, Xuan F-Z (2009) Analysis of second-harmonic generation of Lamb waves using a combined method in a two-layered solid waveguide. J Appl Phys 106:024902. doi: 10.1063/1.3171942

[13] Müller MF, Kim J-Y, Qu J, Jacobs LJ (2010) Characteristics of second harmonic generation of Lamb waves in nonlinear elastic plates. J Acoust Soc Am 127:2141-2152. doi: 10.1121/1.3294714

[14] Matsuda N, Biwa S (2011) Phase and group velocity matching for cumulative harmonic generation in Lamb waves. J Appl Phys 109:094903. doi: 10.1063/1.3569864

[15] Xiang Y, Deng M. Xuan F-Z, Liu C-J (2011) Cumulative second-harmonic analysis of ultrasonic Lamb waves for ageing behavior study of modified-HP austenite steel. Ultrasonics 51:974-981. doi: 10.1016/j.ultras.2011.05.013

[16] Deng M, Wang P, Lv X (2005) Experimental observation of cumulative second-harmonic generation of Lamb-wave propagation in an elastic plate. J Phys D: Appl Phys 38:344-353. doi: 10.1088/0022-3727/38/2/020

[17] Deng M, Yang J (2007) Characterization of elastic anisotropy of a solid plate using nonlinear Lamb wave approach. J Sound Vib 308:201-211. doi: 10.1016/j.jsv.2007.07.029

[18] Deng M, Xiang Y, Liu L (2011) Time-domain analysis and experimental examination of cumulative second-harmonic generation by primary Lamb wave propagation. J Appl Phys 109:113525. doi: 10.1063/1.3592672

[19] Matlack KH, Kim J-Y, Jacobs LJ, Qu J (2011) Experimental characterization of efficient second harmonic generation of Lamb wave modes in a nonlinear elastic isotropic plate. J Appl Phys 109:014905. doi: 10.1063/1.3527959

[20] Liu Y, Chillara VK, Lissenden CJ (2013) On selection of primary modes for generation of strong internally resonant second harmonics in plate. J Sound Vib 332:4517-4528. doi: 10.1016/j.jsv.2013.03.021

[21] Gol'dberg ZA (1960) Interaction of plane longitudinal and transverse elastic waves. Sov Phys Acoust 6:307-310.

[22] Jones GL, Kobett DR (1963) Interaction of elastic waves in an isotropic solid. J Acoust Soc Am 35:5-10. doi: 10.1103/PhysRev.136.A411
[23] Landau LD, Lifshitz EM (1959) Theory of Elasticity. Pergamon Press, New York
[24] Norris AN (1998) Finite-amplitude waves in solids. In: Hamilton MF, Blackstock DT (eds.) Nonlinear Acoustics, Academic Press, New York, pp 263-277
[25] Auld BA (1973) Acoustic field and waves in solids, Wiley, London
[26] Smith RT, Stern R, Stephens RWB (1966) Third-order elastic moduli of polycrystalline metals from ultrasonic velocity measurements. J Acoust Soc Am 40:1002-1008. doi: 10.1121/1.1910179
[27] Matsuda N, Biwa S (2012) A finite-difference time-domain technique for nonlinear elastic media and its application to nonlinear Lamb wave propagation. Jpn J Appl Phys 51:07GB14. doi: 10.1143/JJAP.51.07GB14
[28] Graves RW (1996) Simulating seismic wave propagation in 3D elastic media using staggered-grid finite differences. Bull Seismol Soc Am 86:1091-1106.